Technische Universität München
Fakultät für Physik

Bachelor Thesis in Physics

Time Resolution and Radiation Damage Analysis for the HADES Pion Beam Trackers

Jan Macháček

August 11, 2011

Advisors: Rafał Lalik,
Prof. L. Fabbietti

Contents

Introduction

The **H**igh **A**cceptance **D**i-**E**lectron **S**pectrometer (HADES) detector located at SIS18[1] at the GSI Darmstadt[2] allows fixed target experiments through proton and ion collisions with beam energies up to 3.5 AGeV. The main intent is the analysis of hadron properties at high temperatures and densities.

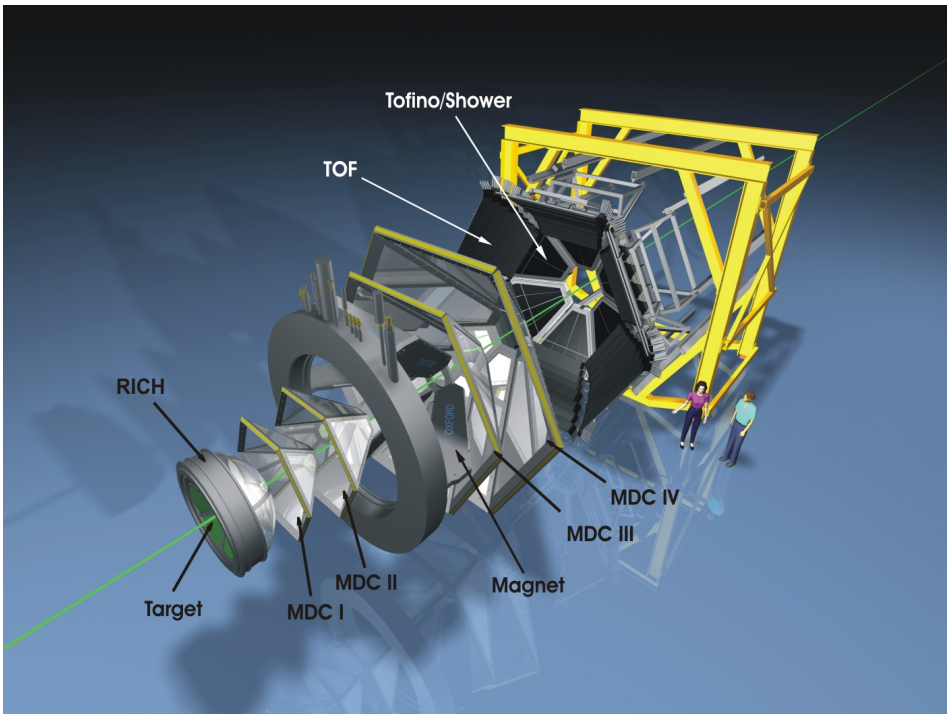

Figure 1: An exploded view of the HADES detector located at the GSI Darmstadt (A. Schmah, HADES collaboration).

The detector itself consists of three major components, all of which are lined up behind the target and cover polar angles from 18° to 85°, while providing full coverage of the azimuthal angle. First in line, the RICH detector[3] is hadron blind. It is used to detect electrons as well as an on-line trigger for these particles. The following sets of MDC[4] in conjunction with the magnetic field allow for tracking and energy loss particle identification. The final part, consisting of the Shower and TOF detectors[5], is used for particle recognition by time-of-flight measurements (figure 1).

[1] **S**chwer**I**onen**S**ynchrotron - Heavy ion synchrotron.
[2] GSI Helmholtzzentrum für Schwerionenforschung GmbH.
[3] **R**ing **I**maging **CH**erenkov detector.
[4] **M**ultiwire **D**rift **C**hambers
[5] Two different **T**ime-**O**f-**F**light detectors are being used for different azimuthal angles.

The creation of new infrastructure for FAIR[6] opens up new possibilities for HADES, allowing experiments with heavy ions at energy levels up to 8 AGeV. To explore the full potential available at HADES, preparations for pion beam experiments are in progress. The usage of a pion beam implies the design of a new beam tracking method. This bachelor thesis concentrates on work aiding the development of this system.

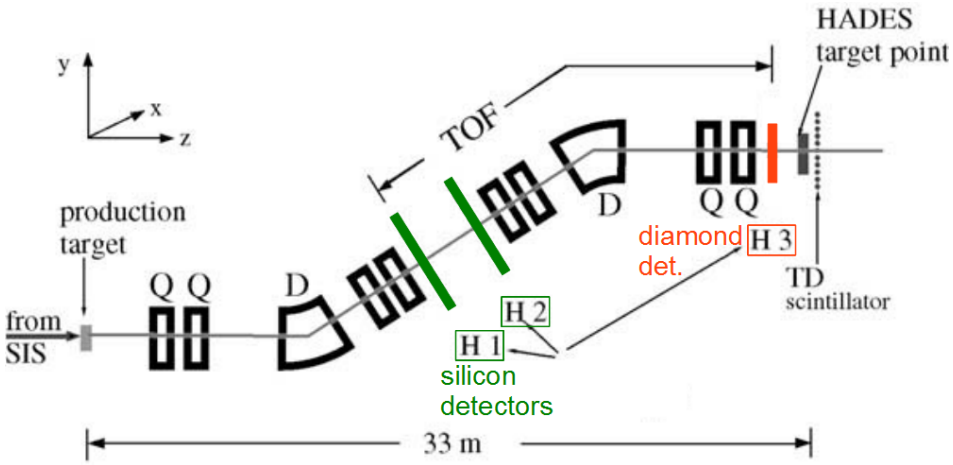

Figure 2: This is an overview over the tracking system, two silicon detectors are positioned at H1 and H2, and the diamond detector is located at H3. A number of quadrupole (Q) and dipole (D) magnets are used for focusing (J. Diaz, [1]).

Pion beams are secondary beams which are produced colliding high intensity ($N \sim 10^{11}$ particles/s) proton or nitrogen beams on a Be target. During a high intensity beamtime (August 2005) a primary beam of $4 - 5 \cdot 10^{10}$ nitrogen atoms per spill [7] with energies of about 2 AGeV has been impinged on a beryllium target. The pion beam is not monoenergetic due to the nature of its creation, delivering pion beam intensities of $1.8 \cdot 10^6$ per spill at momenta of ≈ 1.2 GeV/c [2]. This successful test had shown the feasibility of such a secondary beam at SIS18.

The beamline chicane (figure 2) which starts from the Be target and finishes at HADES is composed of multiple quadrupole magnets for focusing and two dipole bending magnets. The acceptance in the momentum space for the produced pions is $\frac{\Delta p}{p} \approx 10\%$ which allows beams with rather large intensities, but limits the possibility of having exclusive measurements. For this purpose a resolution of 0.5% is required on the momentum of the pion beam. In order to omit reducing the beamline acceptance and preserving high beam intensities, the momentum of each pion has to be determined very precisely. For this purpose the beam tracking system will be employed. The system is composed by two position sensitive silicon detectors placed at the dispersive plane of the beam. The position measurement of the beam particle at the dispersive plane in conjunction with the bending force of the magnets allows for momentum determination. Figure 3 a) shows a sketch of the dispersive plane in the beam line. The two silicon detectors H1 and H2 measure the position perpendicular to the beam which allows the derivation of momenta. A linear relation between the change in momentum $\Delta p/p$ and

[6] **F**acility for **A**ntiproton and **I**on **R**esearch, located at the GSI.
[7] One 4 second cycle consists of 2 seconds beam time and 2 seconds idling.

the position on the x-axis was determined with a 1.6 GeV proton beam. Hereby variation of the magnetic fields was used instead of variation of the proton momentum [1].

In figure 3 b), position correlation between the two silicon detectors can be seen. Intentional dispersion of particles only takes place along the x-axis.

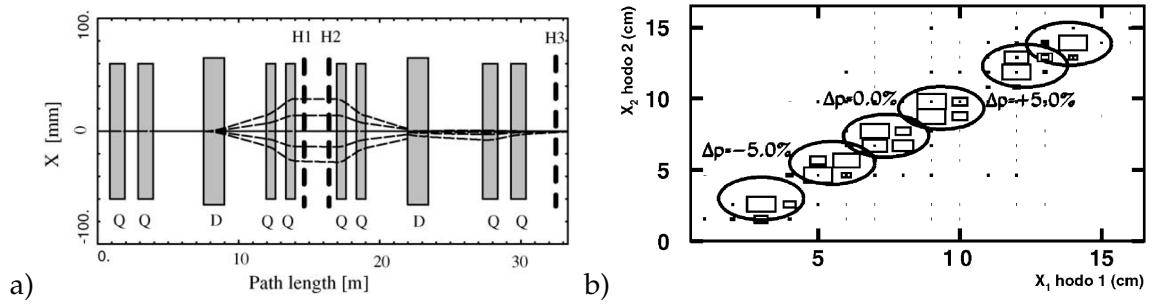

Figure 3: a) Illustrates the function of the dispersive plane. Dipole magnets defocus the beam for analysis in silicon detectors H1 and H2. The beam is split according to its constituent momenta by the beam optics. b) shows the positional correlation between these two detectors. Figures by J.Diaz [1].

Due to their direct placement in the beam, another characteristic of these silicon detectors should be radiation hardness. Indeed particle intensities up to 10^8 part/sec could hit the silicon detectors. Realistic simulations are currently on-going to provide the upper limit of the expected flow on the detector, which was not measured up to now. The analysis conducted in chapter 2 will focus on this issue.

The second part of the tracking system is a diamond detector which is placed in front of the HADES target. It is used for coincidence measurements to ensure a certain pion reaches this destination. It will also provide a very precise ($\sim$ 100 ps) time signal, which is required in order not to spoil the excellent time resolution of the RPC time-of-flight detector in HADES ($\sigma \sim 100$ ps) and will be discussed in the following chapter.

Although consisting of different materials and serving different purposes, the method of signal gereration is very similar for both detectors. A semiconductor detector, such as the silicon detctor, functions in its simplest form as a diode, consisting of a p-n-junction. It is operated in a reverse bias mode, where it ideally should not conduct any current. In this state a particle passing through the detector may deposit energy in the detector through ionization. This creates a significant number of electron-hole pairs, which are free to follow the electric field. This increase in the current is then registered by the amplifiers and turned into an adequate signal. However, a semiconductor always contains a number of minority charge carriers which still allow a leakage current to flow. This current increases for higher carrier mobility, which in turn strongly depends on the operating temperature [3]. The leakage current interferes with the measurement and should be kept as low as possible.

A diamond detector on the other hand is an intrinsic insulator and has no free charge carriers. Radiation is able to ionize this material as well, and the resulting electron-hole pairs benefit from the high charge mobility in diamond [4]. The application of an external electric field allows for a current to flow. The readout is then similar to the one mentioned before, although here leakage currents can be neglected at room temperature [5].

Unfortunately nowadays the maximal size of diamond devices is limited to 1 cm $\times$ 1cm and the costs are too high and favor the usage of a thin silicon detectors to cover large areas (10 cm $\times$ 10cm in this specific application).

Chapter 1

Diamond detector time resolution analysis

This chapter concerns the analysis of the prototype diamond start detector for HADES. As a beam detector, its purpose is to monitor the beam intensity and also to deliver a very precise (order of 100 ps) time signal. Through its direct placement in the beamline, the detector is also subject to high radiation intensities of 10^6 pions/spill. Diamond detectors have proven to be a suitable solution for applications of this kind due to their structure, with a radiation hardness of about one order of magnitude over silicon detectors for energies over 0.1 GeV [5]. The large gap between valence and conduction band of diamond[1] also surpresses thermal noise very well, although diminishing the signal significantly. An excellent signal to noise ratio is needed, because the pions with energies from 1 GeV to 1.7 GeV can be classified as minimal ionizing particles (MIPs), therefore depositing a minimal amount of energy in the diamond. The detector also fulfills the necessary time resolution with its peaking time being at the order of ten ps. This analysis concerns the time resolution of a system of *two* diamond detectors. Data were collected at the COSY[2] facility in Jülich with a proton beam of 2.95 GeV.

1.1 Diamond Detector

The diamond detector itself consists of one layer (500 µm) of monocrystalline diamond, sized 4.7 mm × 4.7 mm and is metallized with 50 nm of chrome and 150 nm of gold. It is divided into 8 sectors, of which each corresponds to a readout channel, as shown in figure 1.1.

The experimental setup used for the test at COSY is shown in fig. 1.2. A proton beam of 2.95 GeV is used in this beamtime. First, the beam passes a veto detector composed of 4 scintillators around a hole of 2.0 cm × 2.0 cm that are used for focusing. The beam then interacts with the diamond detectors, and after moving through the detectors for FOPI and the silicon detector, the beam hits the 2 plastic scintillators sized 4.1 cm × 4.1 cm and 1.0 cm × 1.0 cm. Only the signal of the larger scintillator is used for triggering.

[1] Electron-hole production energy of 13 eV.
[2] COSY: **Co**oler **Sy**nchrotron.

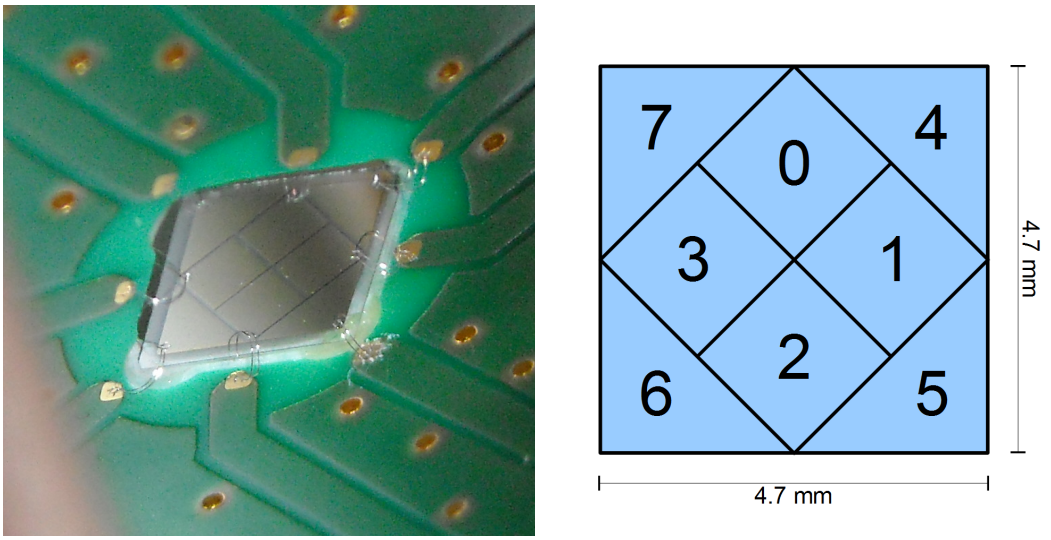

Figure 1.1: Photograph (J.Pietraszko) and sketch of the diamond detector. The sectioning is clearly visible, the central sectors being channels 0-3 and the outer ones corresponding to channels 4-7.

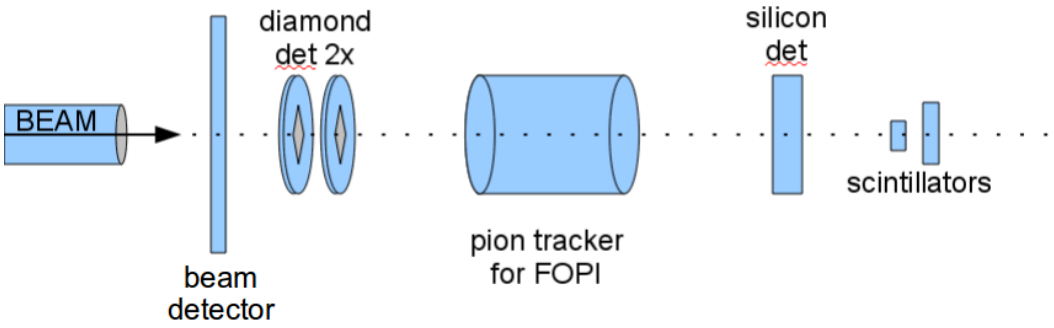

Figure 1.2: The beamtime setup at COSY in Jülich with a 2.95 GeV proton beam.

1.2 Electronic Readout

The 8 detector channels go through different stages of amplification, readout boards with discrete components, specifically a preamplifier, a booster for shaping and time-over-threshold processing as well as a digitizer [6]. Analog signals from the detector are converted to square-like digital signals, their width being proportional to the original signal's amplitude. For channels 0-3 of the second detector an additional preamplification stage was used.

This time signal is then sent to the HADES TDC Readout Board (TRB) [7], a board commonly used for detectors at HADES which can be seen in figure 1.3. It is connected to the data acquisition (DAQ) through ethernet and gigabit optical link, and features a Virtex 4 **f**ield **p**rogrammable **g**ate **a**rray (FPGA). The FPGA has a built-in PowerPC core, the ETRAX processor is running Linux. By using four **H**igh **P**recision **T**ime to **D**igital **C**onverters (HPTDCs), the TRB allows for monitoring of 128 channels with a precision of 96 ps in regular mode. In high-precision mode, which is used here, channels are merged in groups of four, leading to a resolution of 24.41 ps at 32 available channels (8 per TDC) [4]. Every HPTDC is able to process up to 10 signal pulses per event, capture being initiated by trigger signals.

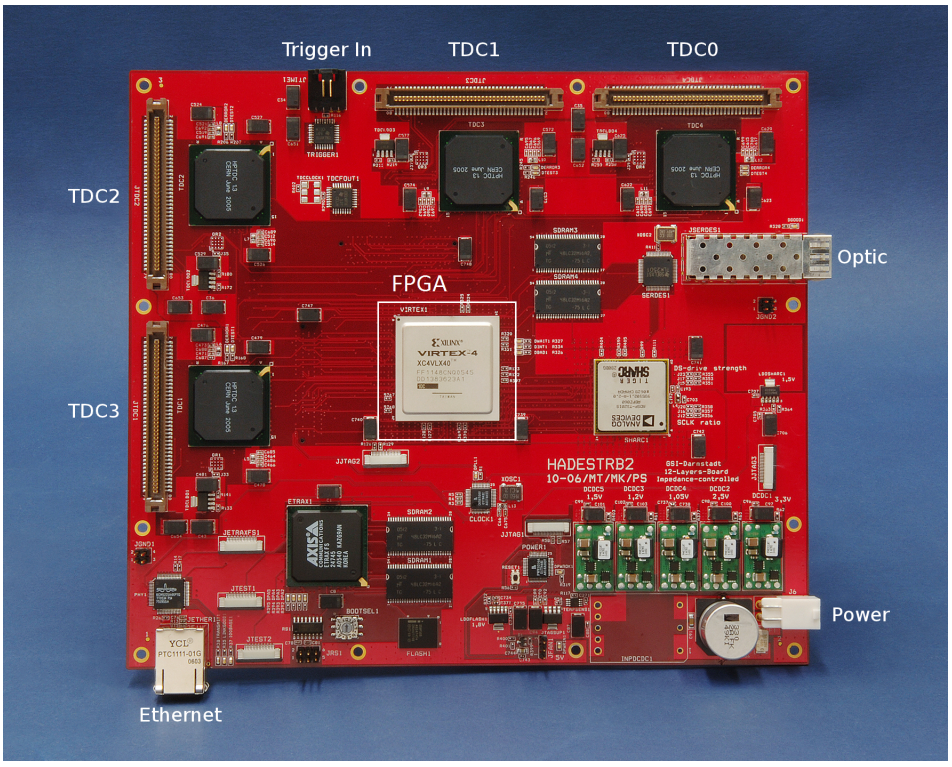

Figure 1.3: HADES TRB board. The four black integrated circuits are the TDCs. The Virtex 4, positioned in the center, is the core FPGA device[7].

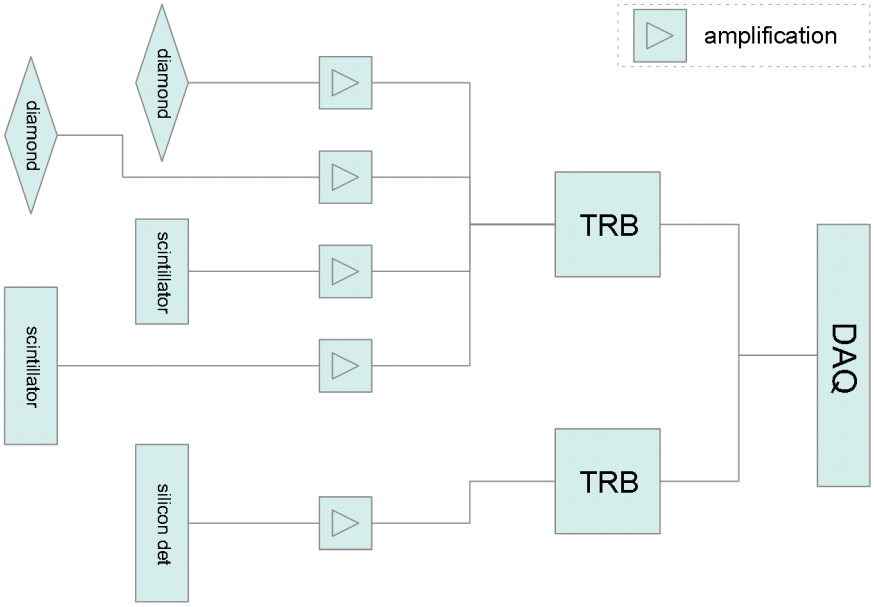

Figure 1.4: Visualisation of the data capture by data acquisition during the Jülich beamtime.

1.3 DAQ System

The complete data acquisition (DAQ) scheme is depicted in figure 1.4. Each diamond detector is connected to a separate TDC on the same TRB, which again is linked to the DAQ system. Data acquisition contains a **c**entral **t**rigger **s**ystem (CTS), a slow control module and a HUB for data transfer. The two scintillators serve as a trigger, the CTS distributes this signal to all attached TRB units[3] and starts the readout of all the detector systems. Being connected to the same TRB as the diamond detector, the scintillator data can be treated in the same way.

As each TDC works independently, they require synchronization by their TDC readout board. This is accomplished by the TRB generating a common time reference signal, which allows for synchronization during the data analysis. Data acquisition stores the data in the raw **H**ADES **L**ist-mode **D**ata (HLD) format. This file contains all information collected by the system, including data from the silicon detector. It first needs to be decoded using HADES' analysis package HYDRA. Calibration to the TDC values is applied to correct for nonlinear behavior.[4] The extracted file contains events arranged according to ROOT's `TTree` structure[5].

The generated `.ROOT` file contains several information, which have been stored for each event and channel separately. The leading time and the corresponding width of a signal are recorded as well, they are described in figure 1.5. Once the signal surpasses a certain threshold value, the setup stores the leading time value. After dropping back under the threshold, another value, the trailing time, is recorded. The difference of these two values is the signal width.

The purpose of this analysis is to determine the error $\sigma_{\Delta t}$ of the time difference Δt between

[3] Two additional TRBs are used by the silicon detector for the pion tracker.

[4] By driving the TDC and trigger system with uncorrelated signals (white noise) and then modifying these data to the fit the expected flat distribution, a parameter matrix can be obtained. These calibration settings were provided by the HADES group and no further actions were required.

[5] ROOT is an object-oriented analysis framework from CERN. http://root.cern.ch (08/2011).

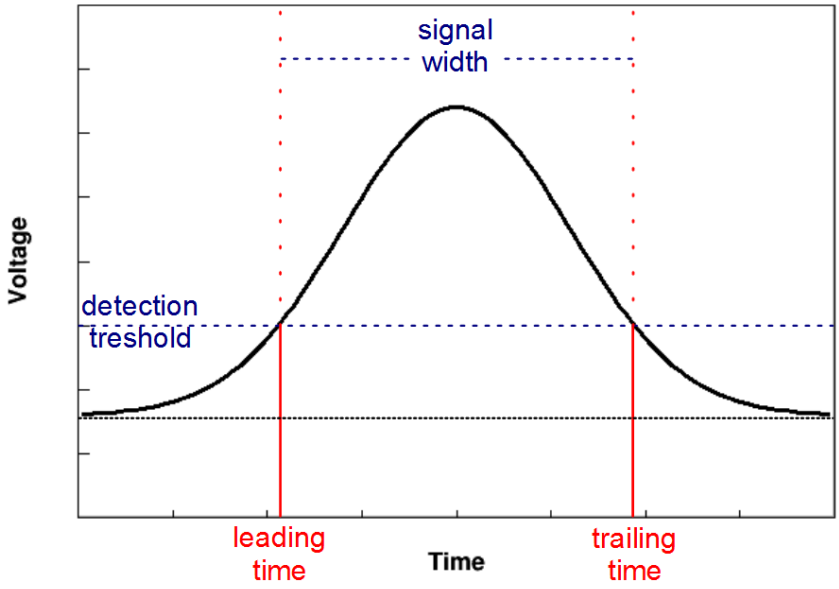

Figure 1.5: Sketch of the detector signal.

correlated channels. The time difference should be constant due to a fixed distance between the two detectors and fixed beam energy. σ_{det1} and σ_{det2} are the absolute time resolutions of the respective detectors and can be deduced from the uncertainty $\sigma_{\Delta t}$.

$$\Delta t = t_2 - t_1 \tag{1.1}$$

$$\sigma_{\Delta t} = \sqrt{\sigma_{\text{det1}}^2 + \sigma_{\text{det2}}^2} \tag{1.2}$$

where t_1 and t_2 are the leading time values measured by detector 1 and 2. The relation for $\sigma_{\Delta t}$ in eq. 1.2 is given by gaussian error propagation. Assuming both detectors have the same resolution $\sigma_{\text{det1}} = \sigma_{\text{det2}}$, this yields

$$\sigma_{\text{det1,2}} = \frac{\sigma_{\Delta t}}{\sqrt{2}} \tag{1.3}$$

Other recorded information include the amount of hits (multiplicity) per strip and module.

1.3.1 Time Spectra

The time spectrum of a channel contains information about its constituent signals. If a channel registers more than one hit per event, the information of the subsequent hits is not considered in this analysis, only the first hit is recorded. If an evenly distributed signal which produces more than one hit per event is captured, more counts should be recorded for lower times. Therefore one would expect uncorrelated noise to follow a descending curve because it has a uniform distribution. An additional signal is added to the 7th channel of each detector by the TRB. This is the time reference, which is used to synchronize data acquisition in order to allow the sorting of hits to their specific events.

Only events with a hit multiplicity larger than 0 are recorded.

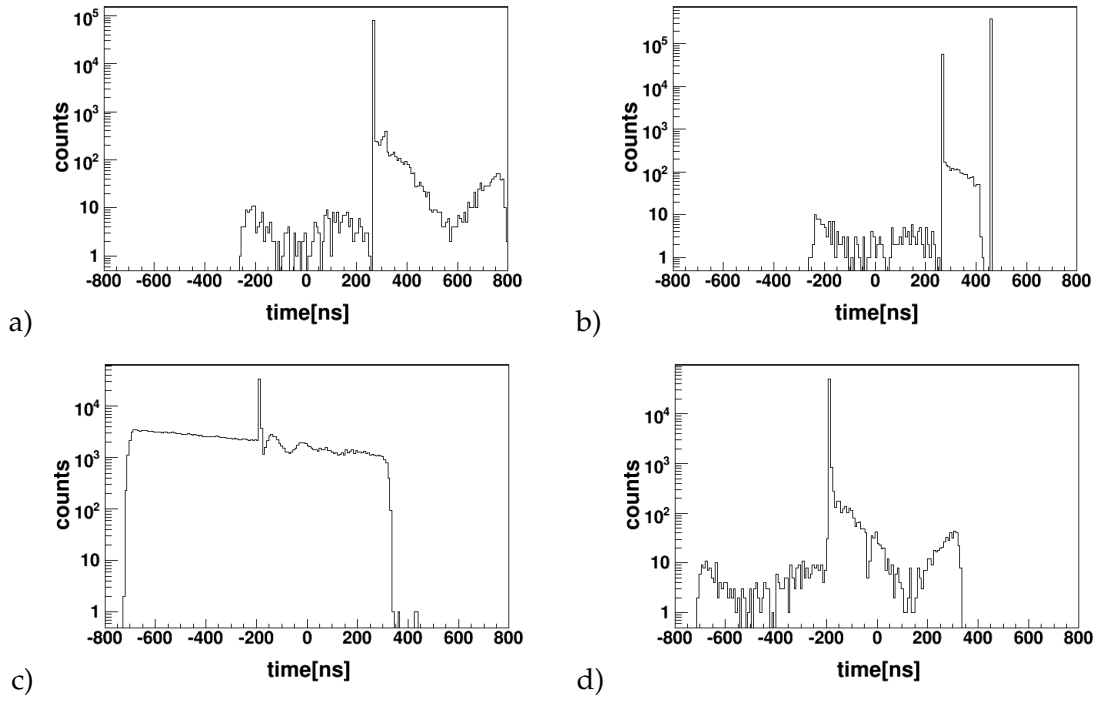

Figure 1.6: Time spectra of single channels. a) represents channels 0-6 on the first detector, b) shows channel 7 of detector 1 with the time reference peak at 460 ns. c) is typical for channels 0-3 of detector 2 with their significant background. d) is an example for channels 4-7 of the second detector.

Figure 1.6 shows the time spectra of this setup for different channels. All channels of the first detector and channels 4-7 of the second detector show a similar structure with a clear data peak and low background noise in fig. 1.6 a), b), d). b) also shows the time reference peak at $\sim$ 460 ns. In c) the first four channels of detector 2 behave differently due to the modified amplification setup, which leads to more noise being captured. Possible candidates for noise are thermal excitations [8] or signals generated by the amplification setup [3]. Nevertheless, a clear peak is still visible as well.

1.3.2 Channel Correlations

In order to run a successful by-channel analysis, it is necessary to know which channels to use for comparison. The channel mapping was not available at this stage, so the channel correlation had to be determined from the data.

When an incoming particle produces a signal on a specific channel of each detector, the hit correlation histogram is filled accordingly. If multiple channels produce a signal, all possible correlations are considered. At this stage, no clear connections can be seen, as there are too many correlations due to noise. The time reference signal is present in each event, therefore it also produces incorrect correlations. These issues are addressed by applying selections on the data. These cuts consist in setting the channel multiplicity to 1, thus removing all events with multiple hits per channel. Additionally, the larger scintillator located at the end of the telescope should register at least 1 hit. The time reference signal has to be removed as well. By allowing only leading time values lower than 440 ns for channel 7 of the first detector, only other signals remain, as can be seen in figure 1.6 b). Channel 7 of detector 2 is treated the same way.

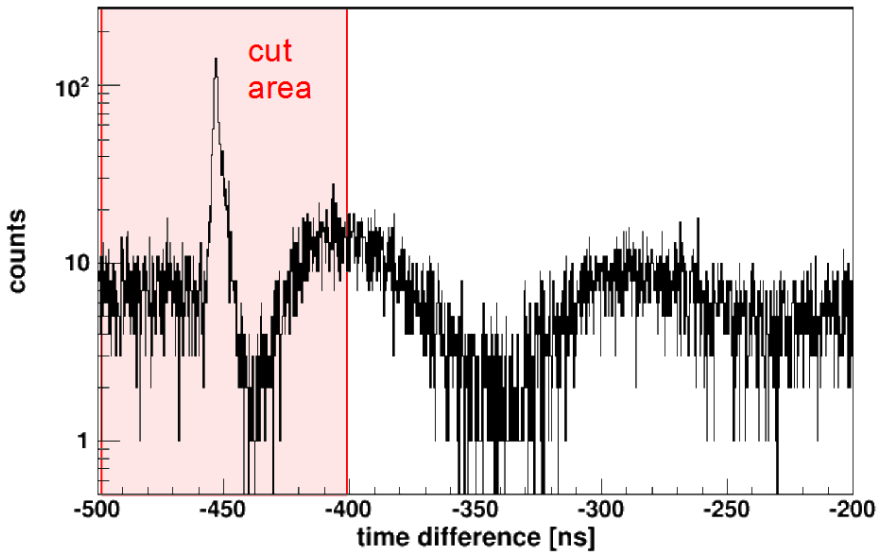

Figure 1.7: An example of a typical time difference graph between two not necessarily correlated channels.

cut 1	channel multiplicity $= 1$
cut 2	scintillator is hit once at least
cut 3	time reference is removed
cut 4	time difference is reduced to values around 50 ns from its peak

Table 1.1: A summary of the cuts in use.

Figure 1.8 a) illustrates the results of this series of cuts, where a correlation is visible for channels 4-7, an example being channel 4 on detector 1 and channel 5 on detector 2. These results prove not to be satisfactory, so an additional cut has to be applied. Due to the fixed

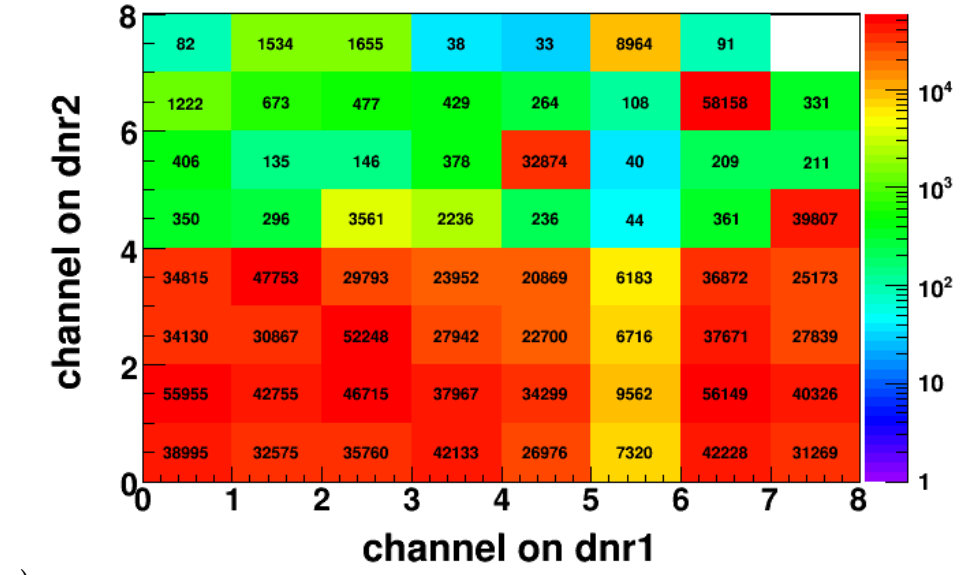

a)

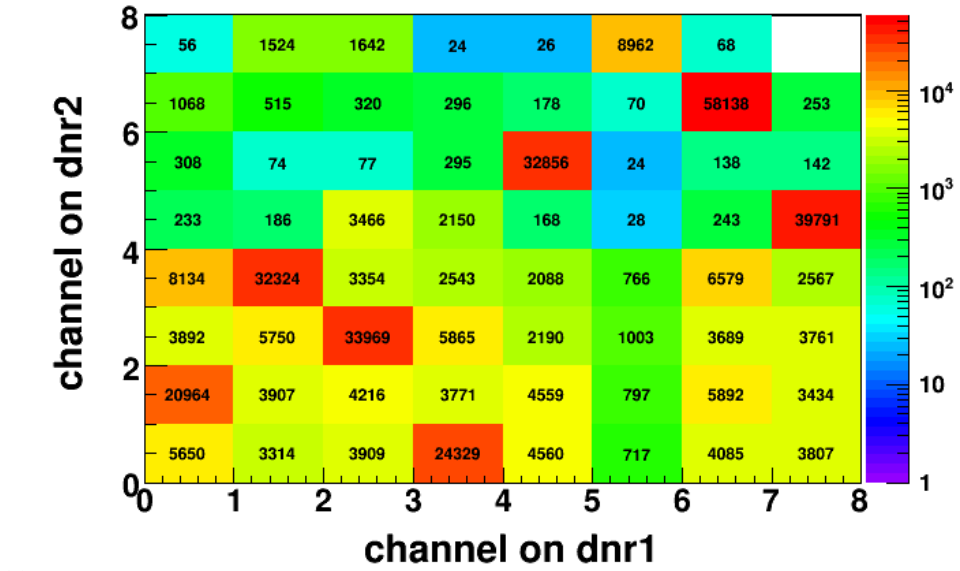

b)

Figure 1.8: a) already shows clear correlationn for channels 5-8 on the second detector after cuts 1-3 (see table 1.1). b) recovers the correlation for all channels after cuts 1-4.

setup all time difference values resulting from incoming particles are expected to peak at a specific point. Figure 1.7 shows the time difference distribution with a notable peak at ~ -450 ns. Therefore a cut leaving ~ 50 ns on each side of the peak is appropriate.

Sharp correlations appear after these cuts, which are summarized in table 1.1, and a pattern between the channels 1-4 appears in fig. 1.8 b), already seen on the upper four channels of fig. 1.8 a). It is notable that there is no correlation between upper and lower channels. The resulting correlation allows the reconstruction of the correct geometrical mapping of the detector channels which is summarized in table 1.2 and fig. 1.9.

channel on first detector	channel on second detector
0	1
1	3
2	2
3	0
4	5
5	7
6	6
7	4

Table 1.2: The channel mapping as it can be read from fig. 1.8 b).

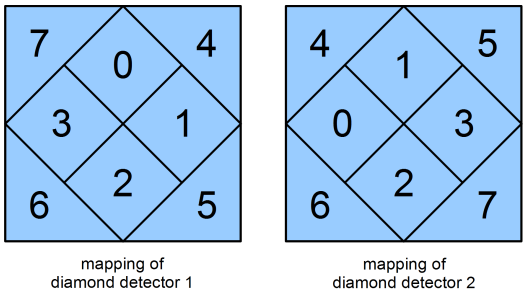

Figure 1.9: A graphical representation of the obtained channel mapping.

1.3.3 Width Distribution

A further investigation into the varying behavior of channels due to noise is allowed through the leading time versus width graphs, as illustrated in figure 1.10, with histograms after cut 1 on the left panels and after cuts 1-4 on the right panels. a) describes all channels of the first detector and shows that time and width are strongly localized, peaking at a particular value. The cuts do not affect the maximum significantly. The upper four channels of the second detector which are shown in c) exhibit the same behavior.

b) shows channels 0-3 of the second detector with a very wide spectrum at lower widths, although a significant peak as in the other channels appears as well. Here a major effect of the cuts is the retention of the peak at (1400 ns, −200 ns) while removing the wide spectrum in b). This spectrum can therefore be clearly attributed to noise and does not contain information relevant to this analysis.

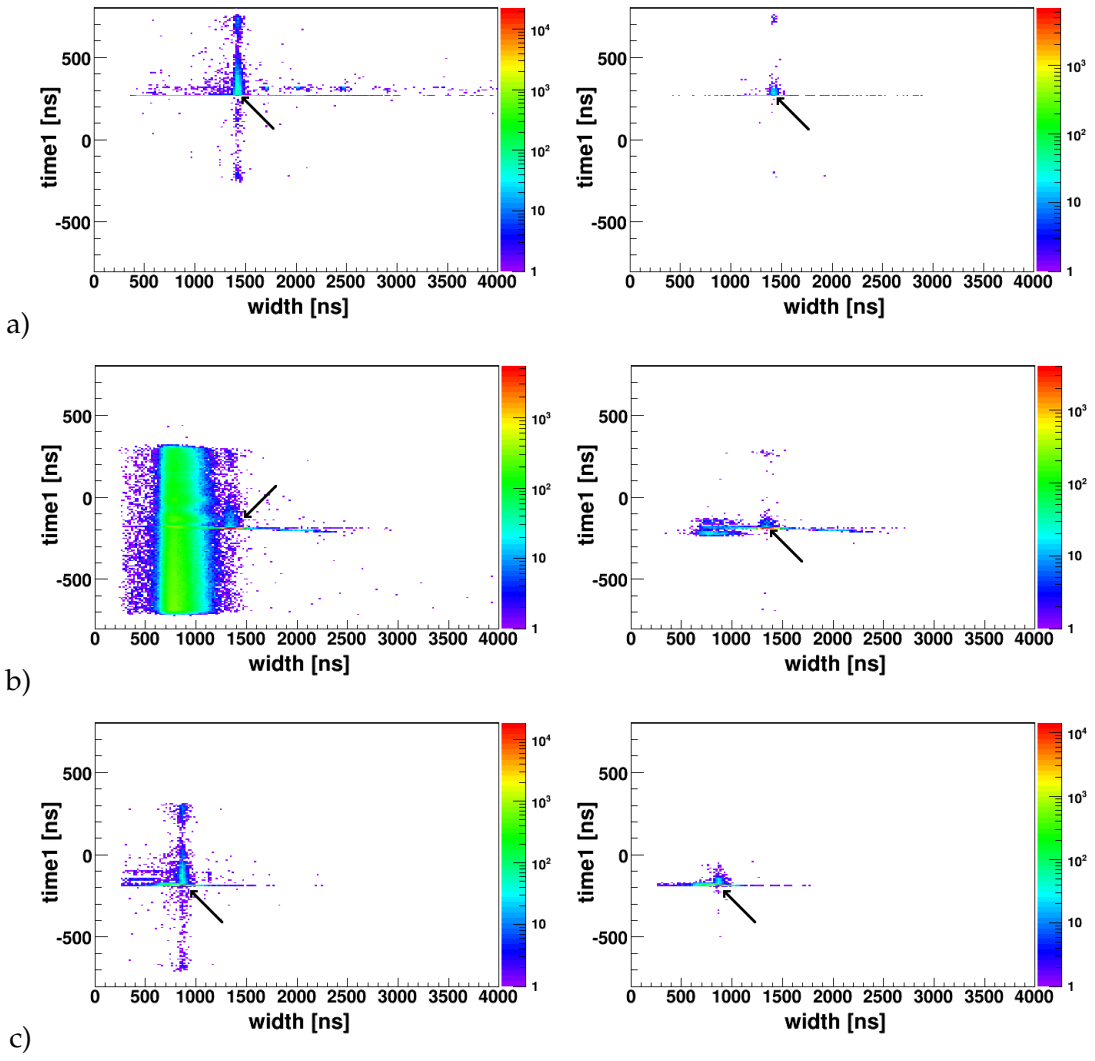

Figure 1.10: a) typical time vs. width graph for all channels of detector 1, b) first four channels of detector 2 and c) channels 4-7 of detector 2. The left histograms only contain cut 1, the ones on the right are after cuts 1-4. Arrows point out the position of the maximum in yield.

1.4 Time Resolution

With knowledge about the channel correlation and signal composition, meaningful time difference graphs can be created. The time reference is excluded for this evaluation. Figure 1.11 shows the yield as a function of the time difference in a) for channels 0-3 and in b) for channels 4-7 with distinctive peaks (~ -455 ns). A gaussian fit through the maximum allows the calculation of its width σ_{setup} and the single detector resolution can be obtained according to equation 1.3.

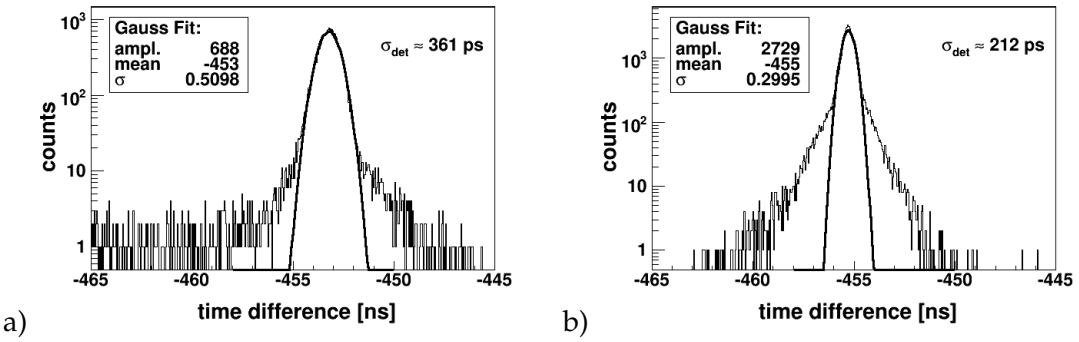

a) b)

Figure 1.11: These are the final results for two representative channels, a) for the group of channels 0-3, b) for channels 4-7. The complete list can be reviewed in table 1.3.

The results strongly depend on the detector segment location. While the channels 0-3 show detector resolutions of approximately 360 ps, analysis of channels 4-7 results in values near 220 ps, the best resolution being 212 ps.

correlated channel pair (det.1 & det.2)	single detector resolution [ps]
0 & 1	367
1 & 3	352
2 & 2	365
3 & 0	361
4 & 5	221
5 & 7	220
6 & 6	212
7 & 4	220

Table 1.3: The resolutions obtained through time difference fits.

These results can be compared to data obtained by the HADES Collaboration in 2009 [9]. Single detector resolutions of 117 ps were determined here for a similar diamond detector with a 1.8 GeV proton beam. This detector had the same dimensions and metallization. Time walk corrections are missing in this analysis, which is the most likely reason for these deviation.

Chapter 2

Silicon detector radiation hardness

Apart from signal creation through ionization, radiation also interacts with the nuclei in the crystal lattice. Generally these effects are undesired and lead to an overall degradation of the detector. This non-ionizing radiation can cause different defects in the crystal lattice of the detector (bulk damage) and defects on the surface. Here a closer look at the damages inside the detector is taken. The main issues are caused by the knock-out of atoms. They lead to defects in the crystal lattice which can have numerous forms.

2.1 Radiation Damages

The dislocation of a single atom, the Frenkel-defect, is possible at energies of around 25 eV, leaving it free to diffuse inside the material at room temperature. These interstitial-vacancy pairs can eventually anneal or diffuse to the surface, this process is strongly dependent on the temperature. Unstable on their own, multiple Frenkel defects can also merge to form clusters. These constructs consist of agglomerations of point defects, which find themselves bound in a stable, irregular state inside the regular crystal lattice. At sufficient energy transfers (2 keV), defect clusters can be created by the primary knock-on atom directly. The treshold for the creation of multiple cluster defects is 12 keV. Such structures can greatly affect the properties of the detector [10][11].

These effects lead to the creation of energy levels within the band gap. As a result, electron-hole pair creation requires less energy, leading to thermal excitation of the conductive band. This in turn leads to an increase of the leakage current [12].

Changes in the effective doping concentration N_{eff} can be induced due to creation of acceptor-like defects. Additionally, the effects of donors are neutralized by vacancies appearing close to the donor atom. In an n-type silicon, this leads to a decrease in the doping concentration. After sufficient irradiation, type inversion occurs and the p-n-junction is generated on to the opposite (ohmic) side of the detector (figure 2.1). These modifications of N_{eff}

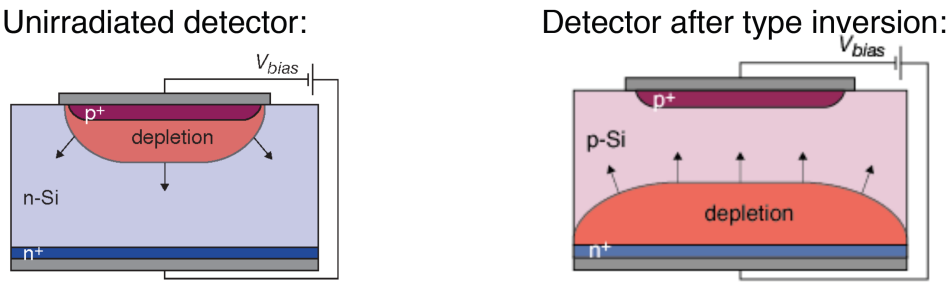

Figure 2.1: Sketch of depletion zone before and after type inversion of an n-type detector (M. Krammer, XI ICFA School on Instrumentation).

cause significant variations in the full depletion voltage V_{fd} [12], since

$$V_{fd} \approx \frac{e}{2\epsilon_0\epsilon_r}|N_{eff}| \cdot d^2, \tag{2.1}$$

where V_{fd} is the depletion voltage, e the elementary charge, d the width of the depletion zone and $\epsilon_0\epsilon_r$ the permittivity of the material in use. As type-inversion does not take place in p-type detectors, the efficient concentration now strictly increases with the fluence Φ, therefore no depletion voltage drops are experienced [13][14]. Fig. 2.2 shows the effective doping concentration N_{eff} as a function of the fluence for 5 n-type and 1 p-type detector. One can see that the n-type values show the characteristic drop which corresponds to type inversion, while the p-type (star symbols) concentration steadily rises. The depletion voltage and effective

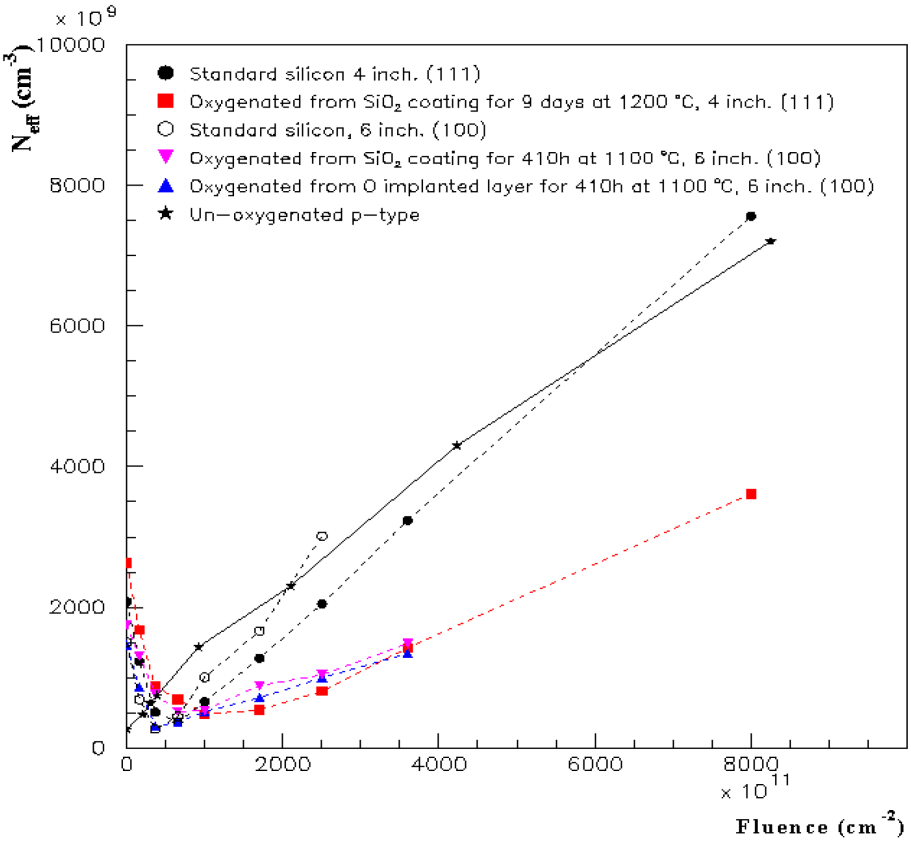

Figure 2.2: Effective doping concentrations N_{eff} ($\propto V_{fd}$) as a function of the fluence for five n-type and one p-type silicon detector (G. Casse, [13]).

concentration are further illustrated in figure 2.3 as a function of the equivalent fluence on a larger scale. The relation between N_{eff} and Φ_{eq} becomes linear for $\Phi_{eq} < 10^{13} cm^{-2}$.

Another result of radiation damage is the trapping and re-emission of charge carriers from cluster defects, leading to an increase in the collection time, therefore distorting the signal. The effect is lower for p-type detectors [13].

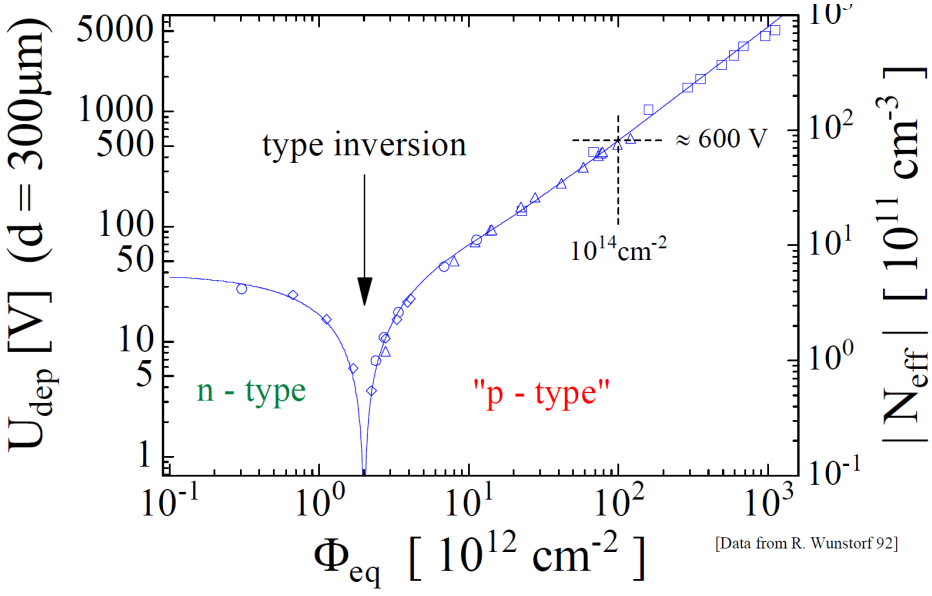

Figure 2.3: The depletion voltage V_{fd} as a function of the equivalent radiation fluence Φ_{eq} during a type inversion, the cross represents the radiation target of parts of CERN's ATLAS detector (G. Lindström, [12], R. Wunstorf, [15])

2.2 NIEL Hypothesis

The **N**on-**I**onizing **E**nergy **L**oss (NIEL) hypothesis predicts the behavior of detectors based on the assumption that structural damages only occur due to non-ionizing energy transfers [3]. These damages generally scale with the fluence, the total number of irradiating particles colliding with the detector. NIEL introduces the hardness factor κ as a measure for the damage done by a particle compared to 1 MeV neutrons, which serve as a general reference.

The original particle fluence Φ can then be expressed in terms of an equivalent neutron fluence Φ_{eq} using equation 2.2:

$$\Phi_{eq} = \kappa \cdot \Phi \tag{2.2}$$

$$\kappa = \frac{1}{D_{\text{neutron}}(1\,\text{MeV})} \frac{\int D_{\text{particle}}(E)\,\phi(E)\,dE}{\int \phi(E)\,dE} \tag{2.3}$$

κ in turn depends on the particle-specific damage function $D(E)$ and the differential flux $\phi(E)$.

$$D(E) = \sum_{\nu} \sigma_{\nu}(E) \int_{0}^{E_{R,\max}} f_{\nu}(E, E_R)\,P(E_R)\,dE_R \tag{2.4}$$

$D(E)$ represents the cross-section for the dislocation of an atom to form a defect. σ_{ν} is the cross-section for the primary atom knock-out reaction, summation over ν accounts for different reaction paths leading to this knock-out. $f_k(E, E_R)$ is the probability for the knocked out particle to obtain an energy E_R if the incoming projectile has an energy equal to E. The partition function $P(E_R)$ indicates the damage done by the knocked-out nucleus and strongly depends on the material in use. Integration runs over possible recoil energies E_R. The neutron reference value is $D_{\text{neutron}}(1\,\text{MeV}) = 95\,\text{MeV mb}$.

The particle beams in this analysis can be considered monoenergetic, therefore $D_{\text{particle}}(E)$ is constant and the integrals in equation 2.3 cancel. Figure 2.4 shows the energy dependent damage functions for different particles in silicon, normalized to the 1 MeV neutron beam. With the hardness factor and fluence, one can then predict the changes ΔI in the leakage current I.

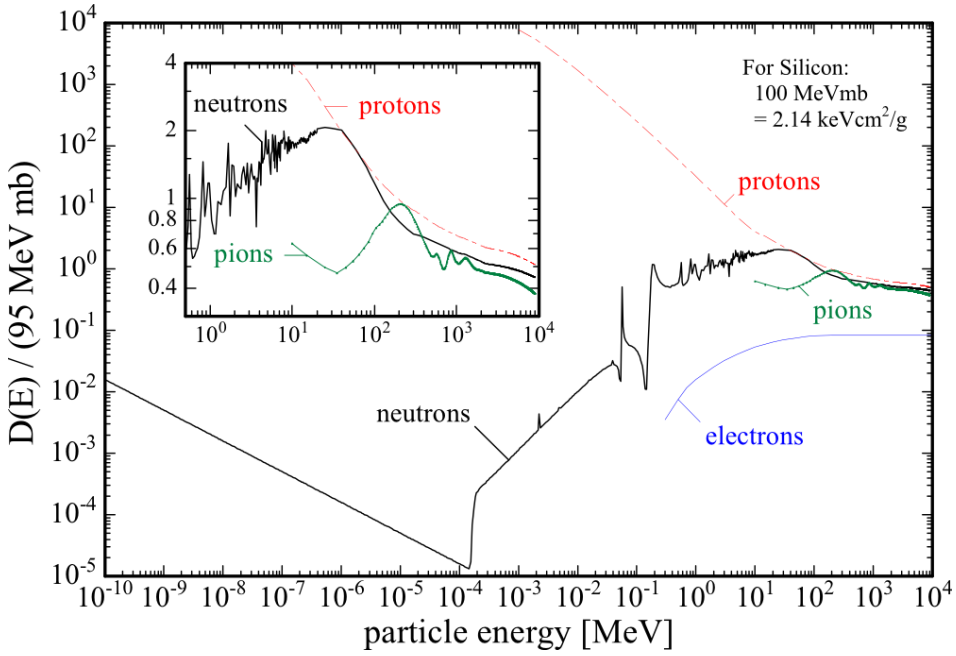

Figure 2.4: The damage functions for different particles in Si. The y-axis is normalized to the 1 MeV neutron beam (G. Lindström, [12]).

$$\frac{\Delta I}{V} = \alpha(t,T) \cdot \Phi_{eq} = \alpha(t,T) \cdot \kappa\,\Phi \tag{2.5}$$

The theoretical increase in I is linear as a function of the fluence Φ. Equation 2.5 also defines the *current-related damage rate* α. It strongly depends on the operating temperature T as well as the time t between irradiation and current measurement during which damages are permitted to anneal. α is largely independent of the material type or irradiating particles [12]. This analysis can now be applied on the tested system.

2.3 Properties and Setup

The detector selected for tracking (figure 2.5.a) is based on a 300 µm deep layer of p-type silicon (figure 2.5.b). Strongly n-doped strips are used to create a large depletion zone in the bulk, even though most of the presently used silicon detectors use the opposite setup [14]. As discussed in section 2.1, this is a promising effort to lower the effects of radiation damage. The detector contains 128 parallel readout strips on each side, with strips on one side being perpendicular to the ones on the other side in order to allow a two-dimensional localization of the incident particle. The total detection area is a square of 10×10 cm^2. For testing, the MLL[1] tandem accelerator is used to supply a proton beam with an energy of 20 MeV.

[1] **M**aier-**L**eibnitz-**L**aboratorium, Garching.

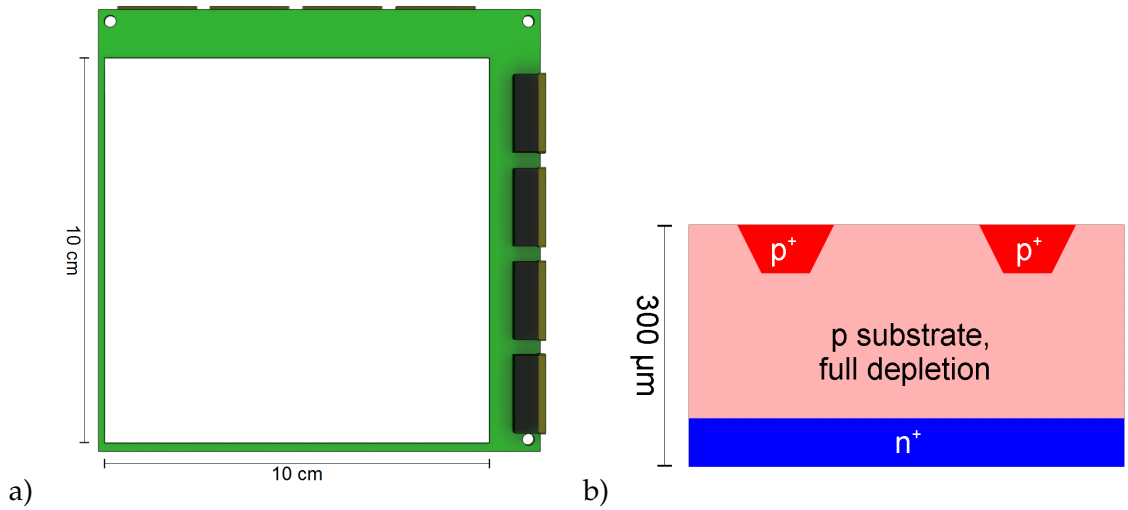

Figure 2.5: a) Model of the silicon detector, b) Cut through the detector, parallel to the n strips and perpendicular to the p strips.

As shown in figure 2.4, protons with 20 MeV kinetic energy correspond to a hardness factor of $\kappa = 2.8$. The operational environment for the silicon detectors at GSI will be mainly influenced by the pion beam. Although the results will be obtained from the proton beam, they can be applied to the HADES setup via the NIEL hypothesis. This is why such a test at the accellerator is useful to characterize the silicon devices.

The beam was focused on an area of $0.25\,\mathrm{cm}^2$. In order to minimize the proton energy loss through interaction with the atmosphere, the detector itself is set up in a vacuum chamber. Photoelectric effects arising from ambient light can also be excluded due to thorough protection from light. The final part of the beamline consists of a scintillator, which delivers the fluence statistics. This setup is sketched in figure 2.6.

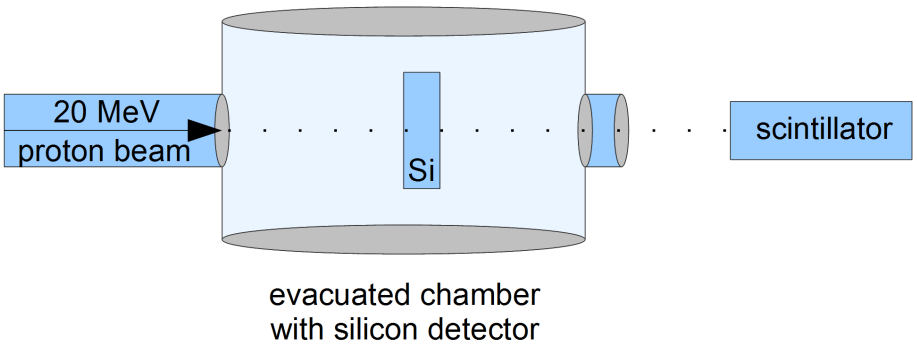

Figure 2.6: The setup used to measure the leakage currents at MLL with the detector in an evacuated, dark chamber.

Power is supplied independently to 4 sectors, each consisting of 32 adjacent channels. The bias voltage is set to 80 V for each part. Only sectors 1 and 2 of the detector are illuminated

due to the low beam size. The detector is also connected to data acquisition for a resolution measurement, not affecting this analysis. The leakage currents[2] I_1-I_4 can now be determined. Readings were taken of the current display of each power supply unit and recorded manually. Additionally, the scintillator delivered the beam intensity statistics through the resolution measurement setup.

2.4 Leakage Currents

Data were collected with different beam rates (20, 80, 350 kHz), the leakage currents were measured while the beam was up. After each irradiation set, read out was continued over time in order to analyze the cool down behavior. Figure 2.7 shows the leakage currents for each sector as a function of time for the three beam rates as well as the currents over the cool down periodes.

The resulting currents exhibit varying behavior. Sectors 3 and 4 barely show any changes as they were not hit by the beam. Solely during the 350 kHz phase sector 4 showed increased leakage current, but then fell back to its base level.

Sector 2 follows the expected rise of currents with larger fluences, while additional cool-down time decreases the currents. Only the 350 kHz beam shows larger discrepancies which could well be connected to the strange behavior of the following sector.

In sector 1, I_1 already starts at an increased level, compared to the other currents. While only showing slight deviations at the lowest beam rate, it enters a steady, almost linear descent during the 80 kHz phase. During the final irradiation, the current fluctuates around the constant level of 1 µA. Even though the first cooldown goes as expected, the following two show the opposite, rising with cooldown time. This unusual behavior might be attributed to a very high sensitivity to the bias voltage and interdependence of the currents.

Taking a closer look on sector 2, the current can also be viewed against the fluence, which has been calculated from the recorded number of particles and the beam size, in figure 2.8. For a qualitative analysis, a simple linear fit is sufficient and errors are not taken into account. According to equation 2.5, the current-related damage rate α can be obtained, using the slope as $\frac{\Delta I}{\Phi}$ and a κ value of 2.8.

$$\alpha = \frac{1}{\kappa \cdot V} \cdot \frac{\Delta I}{\Phi} \approx 9.5 \cdot 10^{-14}\,\mathrm{A/cm} \tag{2.6}$$

The volume $V = 7.5 \cdot 10^{-3}\,\mathrm{cm}^3$ was used here, calculated from the beam spot size and detector thickness.

[2]The measured current actually consists of the leakage current and the current from electron-hole creation, the latter being lower by several orders of magnitude and therefore negligible.

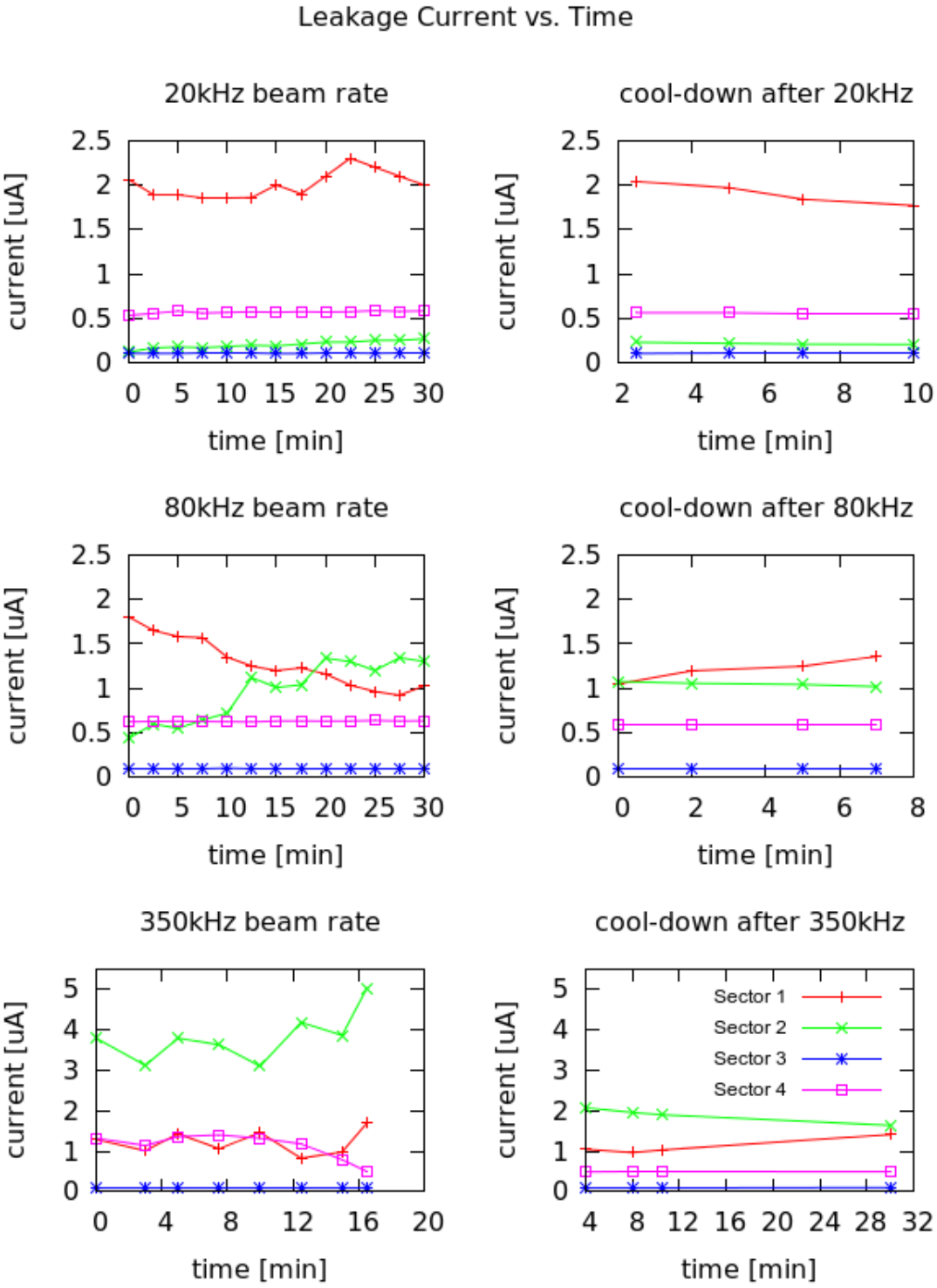

Figure 2.7: These plots show the leakage current vs time at different beam intensities while the beam is online. On the right the cooldown phases between beam times are shown.

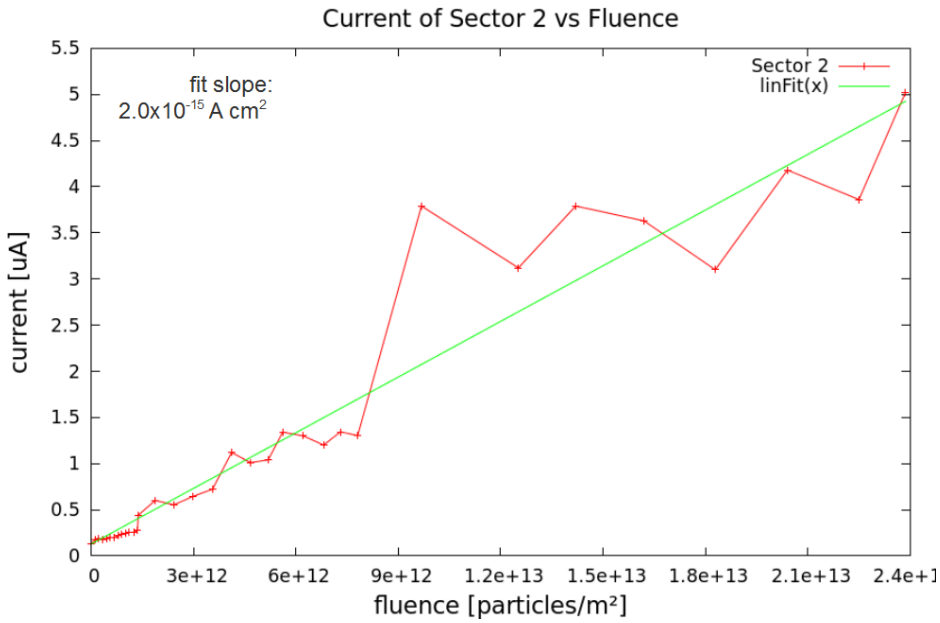

Figure 2.8: The current of the second sector plotted against the fluence. A linear fit approximates the slope in order to calculate the α factor later on.

2.5 Comparison

The increase in the leakage currents for a proton beam of 20 MeV can also be calculated by application of the NIEL hypothesis. To estimate the damages done by this beam, the κ value needs to be determined first. As this is only an approximative analysis, $D(E)$ will not be calculated, but extracted from figure 2.4. For a 20 MeV proton beam this results in the MLL beam being approximately 2.8× as destructive as the reference neutron beam:

$$D_{\text{proton}}(20\,\text{MeV}) \approx 2.8 \cdot D_{\text{neutron}}(1\,\text{MeV}) = 266\,\text{MeV mb} \tag{2.7}$$

$$\kappa_{\text{proton}} = 2.8 \tag{2.8}$$

The predicted current change for the silicon detector used here after a fluence of $\Phi = 2.4 \times 10^9$ particles/cm^2 would be

$$\Delta I = \alpha \cdot \kappa \Phi V \approx 5.0 \cdot 10^6\,\text{cm} \cdot \alpha \tag{2.9}$$

With α values generally at an order of magnitude of 10^{-16} A/cm [10], equation 2.9 yields an estimated current increase of $\Delta I = 5 \cdot 10^{-9}$ A or $5 \cdot 10^{-3}$ µA. This value differs by three orders of magnitude from the values measured at the Maier-Leibnitz-Laboratorium. Apparently the increase in the leakage current must have other causes which supersede the effects of the NIEL hypothesis.

For future developments, it might be interesting to also consider defect engineering techniques such as **D**iffusion **O**xygenated **F**loat **Z**one (DOFZ). This inclusion of impurities can inhibit the creation of relevant defects and has shown promising results with n-type silicon detectors.[12]

Another possible route would be cooling the detector far below room temperature ($\approx 139\,\mathrm{K}$) in order to reduce the required bias voltage and leakage current. It would also diminish reverse annealing, an effect that increases doping concentration after irradiation on a timescale of several months.[8]

Bibliography

1. Díaz, J. *et al.* Design and commissioning of the GSI pion beam. *Nucl. Instr. and Meth. A* **478 (2002),** 511.
2. Lalik, R. in. HADES Collaboration Meeting, Seillec (2011).
3. Lutz, G. *Semiconductor Radiation Detectors* (Springer, 1999).
4. Pietraszko, J. & Koenig, W. in. CBM Collaboration Meeting, Dresden, April 4-8 (2011).
5. De Boer, W. *et al.* Radiation hardness of diamond and silicon sensors compared. *Phys. Status Solidi* **204 (2007),** 3004.
6. Fabbietti, L. *et al.* CERBEROS: a beam tracker system for HADES. GSI Scientific Report (2010).
7. Frohlich, I. *et al.* A General Purpose Trigger and Readout Board for HADES and FAIR-Experiments. *Nucl. Sc. IEEE Trans.* **55 (2008),** 59.
8. Niinikoski, T. O. *et al.* Low-temperature tracking detectors. *Nucl. Instr. and Meth. A* **520 (2004),** 87. ISSN: 0168-9002.
9. Pietraszko, J., Fabbietti, L., Koenig, W. & Weber, M. Diamonds as timing detectors for minimum-ionizing particles: The HADES proton-beam monitor and START signal detectors for time of flight measurements. *Nucl. Instr. and Meth. A* **618 (2010),** 121.
10. Krammer, M. in. XI ICFA School on Instrumentation (2010).
11. Moll, M. in. Radiation effects on electronic components and systems for LHC - CERN Technical Training - 10. April 2000, ROSE Collaboration (2010).
12. Lindström, G. Radiation damage in silicon detectors. *Nucl. Instr. and Meth. A* **512 (2003),** 30.
13. Casse, G., Allport, P. & Hanlon, M. Improving the radiation hardness properties of silicon detectors using oxygenated n-type and p-type silicon. *Nucl. Sc. IEEE Trans.* **47 (2000),** 527.
14. Casse, G. *et al.* First results on the charge collection properties of segmented detectors made with p-type bulk silicon. *Nucl. Instr. and Meth. A* **487 (2002),** 465.
15. Wunstorf, R. *et al.* Results on radiation hardness of silicon detectors up to neutron fluences of 1015 n/cm2. *Nucl. Instr. and Meth. A* **315 (1992),** 149.